High spatiotemporal variation of CH4 and CO2 fluxes from inundated areas in a temperate fen

Johan Emil Kjær[1], Kenneth Thorø Martinsen[1], Theis Kragh[2], Soren Jessen[1], Filippa Fredriksson[1], Lars Baastrup-Spohr[1], Kaj Sand-Jensen[1], Bjørg Friis Michelson[1], and Jonas Stage Sø[2]

[1]University of Copenhagen
[2]University of Southern Denmark

November 16, 2023

Abstract

Peatland ecosystems are unsurpassed in their carbon-storing capacity. However, they can be hotspots for emissions of greenhouse gases (GHGs) depending on soil water saturation and oxygen status. Using automated floating chambers, we investigated the spatiotemporal variability of CH4 and CO2 fluxes and their environmental drivers from inundated areas in a temperate, rich fen. We distinguished between two areas: one with continuous inundation, caused by upwelling groundwater and a lower-lying area with periodic inundation by flooding from an adjacent stream. Using hourly measurements, we found mean effluxes of CH4 and CO2 to be 0.16 and 1.23 g C m-2 d-1 between October and May with more than a 10-fold variation between observations. For CO2, efflux were higher in the periodically inundated area compared to the continuously inundated area. In contrast, CH4 fluxes were higher, and dominated by ebullition, at the area with continuous inundation. Both fluxes increased with soil temperature and wind speed. Advective and diffusive fluxes of CH4 and CO2 associated to groundwater upwelling and upwards diffusion of dissolved gases from shallow groundwater (0.5-0.8 meters below ground level) contributed negligibly to the measured fluxes, suggesting that the emitted GHGs were produced close to the terrain. Our data highlight the large spatiotemporal variation of CO2 and CH4 emissions from fens due to variations in hydrology and topography affecting GHG production near the soil surface. Particularly, the temporary dynamics of soil inundation played a major role in controlling the contribution by CO2 and CH4 to wetland GHG release.

Hosted file

978958_0_art_file_11575328_s3vks2.docx available at https://authorea.com/users/699361/articles/686761-high-spatiotemporal-variation-of-ch4-and-co2-fluxes-from-inundated-areas-in-a-temperate-fen

Hosted file

978958_0_supp_11575075_s3v19m.docx available at https://authorea.com/users/699361/articles/686761-high-spatiotemporal-variation-of-ch4-and-co2-fluxes-from-inundated-areas-in-a-temperate-fen

High spatiotemporal variation of CH_4 and CO_2 fluxes from inundated areas in a temperate fen

Johan Emil Kjær[1], Filippa Fredriksson[2], Kenneth Thorø Martinsen[1], Søren Jessen[2], Bjørg Friis Michelson[2], Theis Kragh[3], Kaj Sand-Jensen[1], Jonas Stage Sø[3] & Lars Baastrup-Spohr[1]

[1]Freshwater Biological Laboratory, Department of Biology, University of Copenhagen, Copenhagen, Denmark, [2]Department of Geosciences and Natural Resource Management, University of Copenhagen, Copenhagen, Denmark [3]Department of Biology, University of Southern Denmark, Odense, Denmark

Key Points:

- Periodic inundation favored CO_2 efflux while continuous inundation led to higher CH_4 efflux in a temperate fen.
- The higher CH_4 efflux from the site with continuous inundation was driven by ebullition.
- Diffusive and advective fluxes from the groundwater contributed negligibly to the total flux of CH_4 and CO_2.

Abstract

Peatland ecosystems are unsurpassed in their carbon-storing capacity. However, they can be hotspots for emissions of greenhouse gases (GHGs) depending on soil water saturation and oxygen status. Using automated floating chambers, we investigated the spatiotemporal variability of CH_4 and CO_2 fluxes and their environmental drivers from inundated areas in a temperate, rich fen. We distinguished between two areas: one with continuous inundation, caused by upwelling groundwater and a lower-lying area with periodic inundation by flooding from an adjacent stream. Using hourly measurements, we found mean effluxes of CH_4 and CO_2 to be 0.16 and 1.23 g C m^{-2} d^{-1} between October and May with more than a 10-fold variation between observations. For CO_2, efflux were higher in the periodically inundated area compared to the continuously inundated area. In contrast, CH_4 fluxes were higher, and dominated by ebullition, at the area with continuous inundation. Both fluxes increased with soil temperature and wind speed. Advective and diffusive fluxes of CH_4 and CO_2 associated to groundwater upwelling and upwards diffusion of dissolved gases from shallow groundwater (0.5-0.8 meters below ground level) contributed negligibly to the measured fluxes, suggesting that the emitted GHGs were produced close to the terrain. Our data highlight the large spatiotemporal variation of CO_2 and CH_4 emissions from fens due to variations in hydrology and topography affecting GHG production near the soil surface. Particularly, the temporary dynamics of soil inundation played a major role in controlling the contribution by CO_2 and CH_4 to wetland GHG release.

Plain language summary

Wetlands with highly organic soil store large amounts of carbon, but they can also release significant amounts of greenhouse gases. To understand this better, we used floating chambers to study how methane (CH_4) and carbon dioxide (CO_2) emissions from water surfaces vary with time and space in a temperate fen ecosystem. One research area was continuously water-covered by upwelling groundwater seepage, and the other was periodically water-covered due to flooding from a nearby stream. We found large variations in the emissions of CH_4 and CO_2. The periodically water-covered area had higher CO_2 emissions, while the continuously water-covered area had higher CH_4 emissions. The low levels of dissolved CH_4 and CO_2 in shallow groundwater (0.5-0.8 meters below ground level) suggested that the emitted greenhouse gases were produced near the surface. Our study highlights how the local hydrology can greatly influence the release of CH_4 and CO_2 from water-covered areas in wetlands, shedding light on an important aspect of greenhouse gas emissions.

1. Introduction

Peatland soils store more carbon relative to surface area than any other terrestrial ecosystem and they contain an estimated 20-30 % of global soil carbon (Leifeld & Menichetti, 2018; Scharlemann et al., 2014; Yu et al., 2010). Peatlands also emit considerable amounts of CO_2 and CH_4 which are the main contributors to the global greenhouse gas (GHG) emission budgets

(Tiemeyer et al., 2020). Despite extensive studies on GHG emissions, it remains difficult to constrain their magnitude due to substantial spatial and temporal variations within and between different peatland ecosystems.

Several physicochemical factors affect GHG emission rates from peatlands. GHG emissions are generally considered higher from nutrient-rich fens than from nutrient-poor bogs due to higher degradability of plant material under nutrient-rich conditions (Moore & Knowles, 1990; Zhang et al., 2021). Microbial activity is highly temperature dependent and soil respiration and methanogenesis is higher in summer than in winter (Yvon-Durocher et al., 2014). Anoxic conditions in waterlogged soils stimulate methanogenesis (CH_4 production) and inhibits CO_2 formation due to lack of oxygen and limited availability of alternative electron acceptors (e.g. nitrate, sulfate and iron-manganese oxides). In contrast, unsaturated conditions enhance soil oxygenation, reduce methanogenesis and stimulate CO_2 production. Furthermore, oxic conditions may facilitate nitrification and formation of iron-manganese oxides and sulfate which may delay methanogenesis when the soil again becomes water saturated (Jerman et al., 2009; Yagi & Minami, 1993). Therefore, peatlands with high topographic heterogeneity and thus a mosaic of unsaturated soil conditions along with intermittently and continuously saturated areas may experience high spatiotemporal variability in CH_4 and CO_2 formation and emission.

Emission of CH_4 may vary by several orders of magnitude over short distances (Wachinger et al., 2000). Unlike CO_2, for which emission is mainly diffusive, CH_4 transport from water and soil to the atmosphere more often follows other pathways. Due to low solubility in water, a large fraction of CH_4 produced in the soil may form bubbles that are released (ebullition). Bubbles bypass possible oxidation by methanotrophs in the oxic surface layer of soil or water and, thereby, increase the net flux compared to a diffusive flux (Sø et al., 2023, SUBMITTED). Thus, ebullition can account for the majority of the total CH_4 flux in several types of wetlands (Stanley et al., 2019; Sø et al., 2022; Villa et al., 2021). Upwelling groundwater rich in CH_4 in wetland soils may generate an advective CH_4 flux, and the depressurizing of oversatured groundwater may additionally promote formation of bubbles at the reduced hydrostatic pressure. Moreover, upwelling groundwater may supply dissolved organic carbon and sulfide, which may consume oxygen and facilitate methanogenesis.

In addition to spatial and seasonal variations, CH_4 and CO_2 fluxes may exhibit diurnal variations. During the growing season, the diurnal dynamics of CO_2 is primarily regulated by light and the balance between photosynthesis and respiration. Outside the growing season and on bare soils, diurnal temperature fluctuations may be pronounced and contribute to the diurnal variation as well. Studies on diurnal variation in CH_4 fluxes show divergent findings with larger effluxes during either day or night or no distinct diurnal patterns (Bansal et al., 2018; Ding et al., 2004; Henneberger et al., 2017; Martin & Moseman-Valtierra, 2017). As these light-dark patterns

likely differ depending on site, peatland type and season, many measurements at high temporal resolution are required for a reliable evaluation of the carbon emission.

Though high spatiotemporal variations in GHG emissions from peatlands call for high-frequency measurements, sampling often takes place infrequently at few locations due to labor-intensive methods and expensive equipment. Recently, automated floating chambers using low-cost sensors have been developed for measurements of GHG fluxes on lakes at high spatial resolution (Bastviken et al., 2020; Martinsen et al., 2018; Sieczko et al., 2020; Sø et al., 2022). The chamber's headspace can be automatically vented between measurements (Sø et al., 2022), which allows hourly measurements of GHG fluxes for several days without inspection. As headspace concentrations of CH_4 and CO_2 are continuously measured, it is possible to quantify both the diffusive and ebullitive gas fluxes. Such floating chambers have not previously been used in water-covered areas of wetlands. Moreover, the CO_2 and CH_4 dynamics of shallow (<30 cm) temporary waterbodies in fens are understudied, particularly in regard to ebullitive and diffusive CH_4 fluxes, despite the large global distribution of temporarily flooded wetlands (Pekel et al., 2016).

While the water table depth at a given time point is important for GHG production, the temporal variation in the water level prior to measurement may play an equally important role (Qian et al., 2022; Tiemeyer et al., 2020). In the present study, we measured GHG fluxes, when the groundwater table is above the ground level, leading to saturated soil conditions. To reflect temporal water level variability prior to measurement, we defined peatland areas with standing water as being subject to either periodic inundation (PI) or continuous inundation (CI). PI may occur when wetland areas with usually unsaturated soils experience flooding by nearby streams. CI may occur when the sum of precipitation and groundwater upwelling equals, or exceeds the sum of evapotranspiration and overland flow. Due to the topographical characteristics and vegetation at the study site, we expected that the continuously saturated area received upwelling groundwater. We predicted that the inundation regime (PI or CI) and soil temperature would be the main drivers of spatiotemporal variability of GHG emission and the partitioning of diffusive and ebullitive CH_4 emission.

Our two specific hypotheses were that: (*i*) continuous soil saturation would favor methanogenesis and higher CH_4 fluxes, while periodic saturation would favor aerobic microbial respiration, higher CO_2 fluxes and lower CH4 fluxes and (*ii*) increasing wind speed and soil temperature would increase both CH_4 and CO_2 fluxes from sites with standing water.

2. Methods

2. 1 Site description

The study was carried out at a 13.2 ha calcareous fen (Elbækengen**)** located in Zealand, Denmark (55.390°N, 12.263°E). The area has a rich floral diversity with several nationally rare species. As a conservation effort, the fen is managed by Denmark's Nature Foundation through cattle grazing during summer and by yearly manual removal of alder (*Alnus glutinosa*). Agricultural land and a small belt of trees to the West and North-West surround the area. To the East, the fen is bordered by Tryggevælde stream. The stream's water level is highly variable throughout the season, as well as controlled by a water lock at the stream's outlet at Køge bay, 6 km downstream. During late autumn to spring, the stream regularly floods large low-lying areas of the fen (Fig. 1d). We distinguish between the lower-lying site with periodic inundation (PI) closer to the stream and the smaller slightly elevated area with continuous inundation (CI) further from the stream (Fig. 1a).

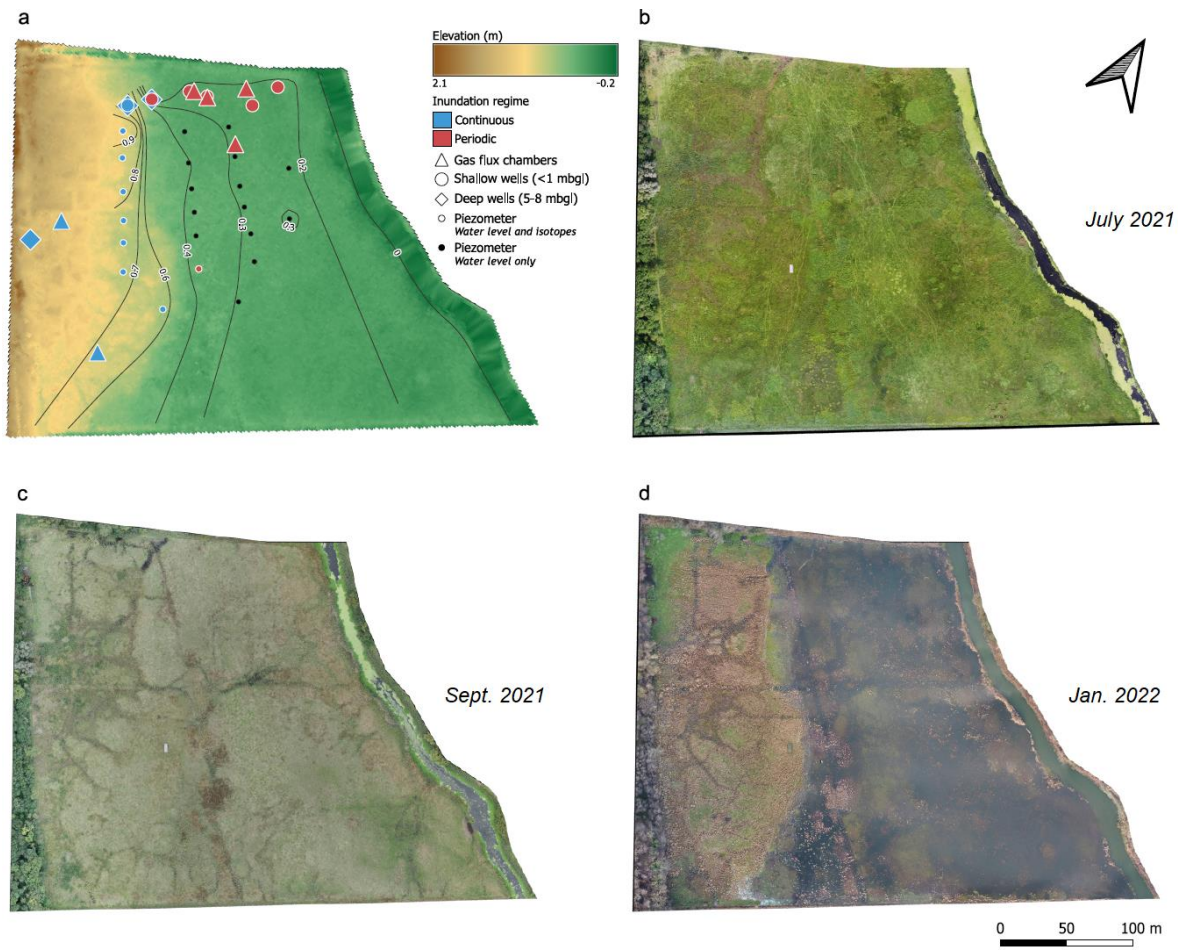

Figure 1. (a) Elevation model with an overview of the placement of sites for chamber based GHG flux measurements (triangles), deep wells sampling regional groundwater (diamonds), and shallow wells and piezometers (circles). Colors indicate the inundation regime as determined from water table variations and stable water isotopes: blue indicates continuous inundation (CI) and red indicates periodic inundation (PI). Filled black circles indicate piezometers in which no

sampling for stable water isotopes was conducted. Black lines indicate hydraulic head isopotential lines drawn for March 2022. Aerial composite photos showing the study site in (b) July 2021, (c) September 2021 and (d) during flooding in January 2022.

2.2 Groundwater sampling and water level monitoring

Six shallow and three deep wells were installed to measure groundwater levels and conduct groundwater sampling for dissolved gases and stable water isotopes (Fig. 1a). The six shallow wells consisted of a 1 m long polyethylene (PEH) 54.6/50 mm OD/ID tube with a 30 cm screen placed at 0.5-0.8 m below ground level (mbgl). The shallow wells were installed using an Ø10 cm casing (Eijkelkamp 01.12.SA Hand bailer auger set) and equipped with a gravel pack (0.9-1.6 mm quartz sand, EN12904) and bentonite-cement sealing from the top of the screen to the surface. In addition, eight piezometer pipes (Ø2.5 cm; white plastic) were installed. As for the shallow wells, the piezometer pipes allowed for water table measurements and shallow groundwater sampling for stable isotopes but not for dissolved gases. The piezometer pipes were pushed into the ground by hand, placing the center of their 12 cm long vertically slotted screens at 0.5 m depth. The three deep wells consisted of 1” galvanized steel pipe with a 10 cm drive-point screen and were installed using a Makita HM1400 pneumatic hammer placing the screen at between 5 and 8 mbgl. The deep wells were used to measure water table depth and to sample for dissolved gases and stable water isotopes in the converging regional groundwater of the catchment discharge zone (i.e. the stream valley).

Groundwater from the six shallow and three deep wells was collected post-clean pumping on the 13th of October 2022 and the 28th of February 2023 using a peristaltic pump and 5/8 mm (OD/ID) PE tubing. Field measurement of pH, dissolved oxygen (O_2) and temperature was done using a Sentix 940 and an FDO 925 WTW electrode mounted in a flow cell. Samples for dissolved CO_2 and CH_4 were collected in pre-evacuated 12 mL Labco Exetainer vials through a syringe needle connected to the pumping tube. The eight piezometer pipes were sampled for stable isotopes of water monthly between September 2021 and March 2022, using a 60 mL PE syringe connected to a 5/8 mm PE tube with a three-way stop-cock. Samples for stable isotopes of water, alkalinity and sulfide were collected in a PE syringe and passed through a 0.20 µm Sartorius Minisart CA filter into respective vials. Sulfide was preserved using Zn-acetate, and all samples were refrigerated until analysis. Dissolved CO_2 and CH_4 were measured on an Agilent 7890A gas chromatograph. Stable water isotopes were measured by a Picarro L2120-i Cavity Ring-Down Spectroscopy (CRDS). Alkalinity was determined by Gran-titration (Appelo & Postma, 2005). Sulfide was determined spectrophotometrically using the methylene blue method (Cline, 1969). Continuous water level measurements, compensated for barometric pressure, were obtained from the six shallow wells using HOBO U20L-04 water level loggers.

2.3 Potential for bubble formation in groundwater

The potential for ebullition was quantified as the bubble formation pressure P_b, defined as:

$$P_b = P_{CO_2} + P_{CH_4} + P_{H_2S} + P_{H_2O} + P_{O_2} + P_{N_2} - P_w - P_{atm}$$

The first six of the right-hand terms are partial pressures of dissolved gases as indicated by subscripts, P_w is the pressure exerted by the water column above the well screen, and P_{atm} is the atmospheric pressure (1 atm). P_{N_2} was assumed to be 0.78 atm, while partial pressures of CO_2, CH_4, H_2O and O_2 were calculated by speciation using PHREEQC (Parkhurst and Appelo, 2013) and the field-measured pH, temperature and alkalinity. In the calculation, P_w was fixed to 0 atm which is equivalent to calculating P_b in the upwelling water for the case where this water has reached the water table. $P_b < 0$ indicates that the external pressure of the water column and the atmosphere exceeds the sum of the dissolved gas partial pressures, implying that bubble formation in the sampled groundwater is not feasible, even if this water should move upwards to reach the water surface. In contrast, $P_b > 0$ indicates that bubble formation is feasible.

2.4 Advective and diffusive groundwater-associated CO_2, CH_4, S^{2-} and O_2 fluxes

For comparison to surface chamber emission measurements (see below), we estimated advective CO_2 and CH_4 fluxes (F_{adv}^{gw}) associated to the upwards movement of groundwater in the CI area. The advective fluxes were calculated from the solute concentrations observed in the shallow well, placed in the CI area, multiplied by the Darcy flux. A range of the Darcy fluxes were applied, derived from hydraulic conductivities of 9.3×10^{-8} to 2.7×10^{-6} m/s (obtained by slug tests; we discarded one high value of 3.2×10^{-5} m/s derived from the river-most screen installed in a sandy levee), along with the range of vertical gradients of 9.1 to 33 ‰ observed between the shallow well and its co-located deep well in the CI area.

In addition, diffusive fluxes (F_{diff}^{gw}) of dissolved CO_2 and CH_4 through the overlying saturated zone to the surface were calculated using Fick's first law. Here, we applied the dissolved concentrations of CO_2 and CH_4 observed at the depth of each individual well screen. To obtain vertical concentration gradients, we assumed equilibrium with the atmosphere's CO_2 and CH_4 partial pressures at the surface. An effective diffusion coefficient of 10^{-9} m^2 s^{-1} and a porosity of 0.5 was applied (Appelo & Postma, 2005).

To investigate the processes controlling shallow redox-conditions, we also calculated upwards advective and diffusive S^{2-} fluxes as above. We also estimated the downwards diffusive O_2 flux assuming a dissolved O_2 concentration at the surface of 0.3 mM, corresponding to equilibrium with the atmosphere's partial pressure of oxygen.

2.5 Meteorological and surface water measurements

Meteorological variables including mean wind speed and gust speed (HOBO S-WSET-A), relative humidity and air temperature (HOBO U23 Pro v2), photosynthetically active radiation

(PAR; 400-700 nm; HOBO S-LIA-M003), atmospheric pressure (HOBO U-20-001-04) and precipitation (HOBO rain gauge, RG3) were measured at a weather station in the fen (Fig. S1). The PAR data were used to distinguish between daytime and nighttime (< 10 μmol $m^{-2} \cdot s^{-1}$).

At each deployment of gas flux chambers (see below), the depth of standing water was measured and soil temperature at 5 cm depth was monitored continuously (using either HOBO UA-002-64 or StowAway TBI32 data loggers). In cases where no soil temperature data was recorded at a certain plot (due to sensor failure or corrupted data), we used the mean of other sensors deployed simultaneously at neighboring plots. The correlation of soil temperatures between neighboring plots was very high (Pearson R = 0.98).

2.6 CH_4 and CO_2 fluxes from water surfaces

To measure CH_4 and CO_2 fluxes we used opaque automated and vented floating chambers as described by Sø et al. (2023). During repeated 60-minute measurement cycles, CH_4 and CO_2 concentrations in the chambers' headspace were logged every 2 seconds for 40 minutes using a small low-cost CO_2 (K33 ELG, Senseair, Sweden) and CH_4 sensor (NGM2611-E13, Figaro, USA). The system is controlled by a microprocessor (Arduino Uno Rev3, USA) and powered by an 18 Ah $LiFePO_4$ battery, which provides sufficient power for deployments for several days. Using a small pump, the chamber headspace is replaced several times with atmospheric air during 20 minutes of venting between the measurement periods. The sensor and ventilation system are an automated, updated version of a design originally described by Bastviken et al (2020) and applied by Seiczko et al. (2020). A similar automated floating chamber system has previously been applied for CO_2 measurements (Martinsen et al., 2018).

Four chambers were deployed during six campaigns lasting 2-6 days between October 2021 and May 2022. Chambers were placed at six different plots, with two CI and four at PI. The number of plots reflected the relative area of the two types of inundated sites (Fig 1a). We always placed two chambers at each site type, but we randomized the chosen plots at PI. The CO_2 data were supplemented by manual chamber measurements in early summer 2021.

2.7 Flux calculation

We calculated diffusive and total CH_4 fluxes as well as diffusive CO_2 fluxes (g C m^{-2} d^{-1}). In total, we obtained CH_4 and CO_2 data from 1674 hourly cycles. First, we applied a 10-point moving average of the raw data to reduce the noise due to the low bit analog-to-digital converter of the Arduino Uno (Kajiura & Tokida, 2021; Stage Sø et al., 2022). Secondly, we calculated diffusive fluxes, using linear regression to calculate the slope of CH_4 and CO_2 concentration over time. Fluxes were calculated as:

$$F(t) = \frac{\Delta C}{\Delta t} \frac{V\,P}{R\,K} \frac{1}{A}$$

Where $\frac{\Delta C}{\Delta t}$ is the concentration change of the gas over time in seconds (i.e. the slope of the regression model), V is the volume of the chamber (L), P is pressure (atm), R is the universal gas constant (L atm K^{-1} mol^{-1}), K is the temperature (in ^{o}K) and A is the chamber footprint (m^2). To avoid artifacts from the headspace exchange during the ventilation phase, we used a dead-band of 250 seconds after venting. The following 750 seconds were used for the regression analysis. The data quality was ensured by an initial sorting according to the explained variance, keeping models with $R^2 > 0.9$. Each measurement was also visually inspected. When calculating diffusive CH_4 fluxes, 722 out of 1674 cycles where discarded due to low R^2 or ebullition events in the timeframe used for regression, resulting in 952 diffusive CH_4 fluxes. For CO_2, 472 measurements were discarded and 1257 accepted.

To identify measurement cycles with ebullitive events at any part of the cycle (expect for the initial dead-band), we calculated the running difference between each data point with 2 ppm as a threshold indicating a bubble entering the chamber headspace. Combined with a visual inspection of each measurement, we found a total of 453 measurements with ebullition events. For cycles with ebullition, we calculated the total CH_4 flux (ebullition + diffusion) by subtracting the maximum CH_4 concentration during the measurement cycle from the minimum concentration and dividing it by the total time elapsed in the measurement cycle, thus obtaining a concentration change per unit time (ppm s^{-1}) equivalent to the slope of the linear regression line. Ebullition events would typically lead to a slight peak followed by a quick decrease to a more steady level. This phenomenon is due to incomplete mixing before the bubble is homogeneously mixed in the chamber's headspace (Barbosa et al., 2021). To avoid overestimation due to this phenomenon we used the CH_4 concentration attained 60 seconds after the bubble peak unless the maximum concentration was observed less than 60 seconds before the measurement cycle ended, in which case we used the maximum concentration instead.

2.8 Statistics

For the full flux dataset, we used unequal variance t-test (Welch's t-test) to test for overall differences in fluxes of CO_2, diffusive and total CH_4 between CI and PI as well as diurnal variation between day and night.

The subset of data containing all environmental variables (570 and 720 observations for CH_4 and CO_2) was used for further modeling. To identify potential drivers of CO_2, total and diffusive CH_4 flux, we fitted linear mixed-effects models using the 'lme4' R-package (Bates et al., 2015). Since observations within plots potentially are more similar than between plots, we included 'plot' as a random effect. All models included the continuous predictor variables soil temperature (°C), water depth (cm), wind speed (m s^{-1}) and air pressure (kPa), diurnal phase (day or night) and site (CI or PI) as fixed effects (table 1). The continuous predictor values were standardized by subtracting the variable's mean and dividing it by the standard deviation. Before modeling, Spearman rank correlations were used to investigate co-variance between continuous predictor

variables. When the correlation coefficient exceeded ± 0.40 we excluded one of the variables (Fig. S5-S7). The model fits were verified using diagnostic plots (Fig. S2-S4). We calculated 95 % confidence intervals of the estimates using parametric bootstrapping with 1000 simulations. We consider estimates with 95 % confidence intervals not overlapping zero as significant results. Marginal R^2, representing variance explained by fixed effects and conditional R^2, which include both fixed and random effects, were calculated for each model using the R package 'MuMIn' (Bartoń, 2023). All data analysis was performed using R statistical software version 4.2.0 (R Core Team, 2023).

3. Results

3.1 Groundwater contribution to saturated conditions

The stable water isotope data show that the deep (5-8 mbgl) groundwater share a similar isotopic signal with the shallow (<1 mbgl) wells and piezometers located in CI (Fig. 2a). In addition, high frequency water level measurements display that the shallow well located in this area experiences a relatively stable water level throughout the measuring period, compared to the low-lying shallow wells located in PI closer to the stream (Fig. 2b). This indicates that the continuous inundation in CI was caused by groundwater upwelling where deep, regional groundwater keeps the hydraulic head high and gives rise to continuously saturated conditions at the surface. In contrast, the wells in the PI area demonstrated fluctuating hydraulic heads during the same period, which seem to vary according to Tryggevælde stream's water level. Their isotopic signal also shows a larger spread, indicating that both stream water and precipitation may be sources of recharge that control the measured hydraulic head in this area.

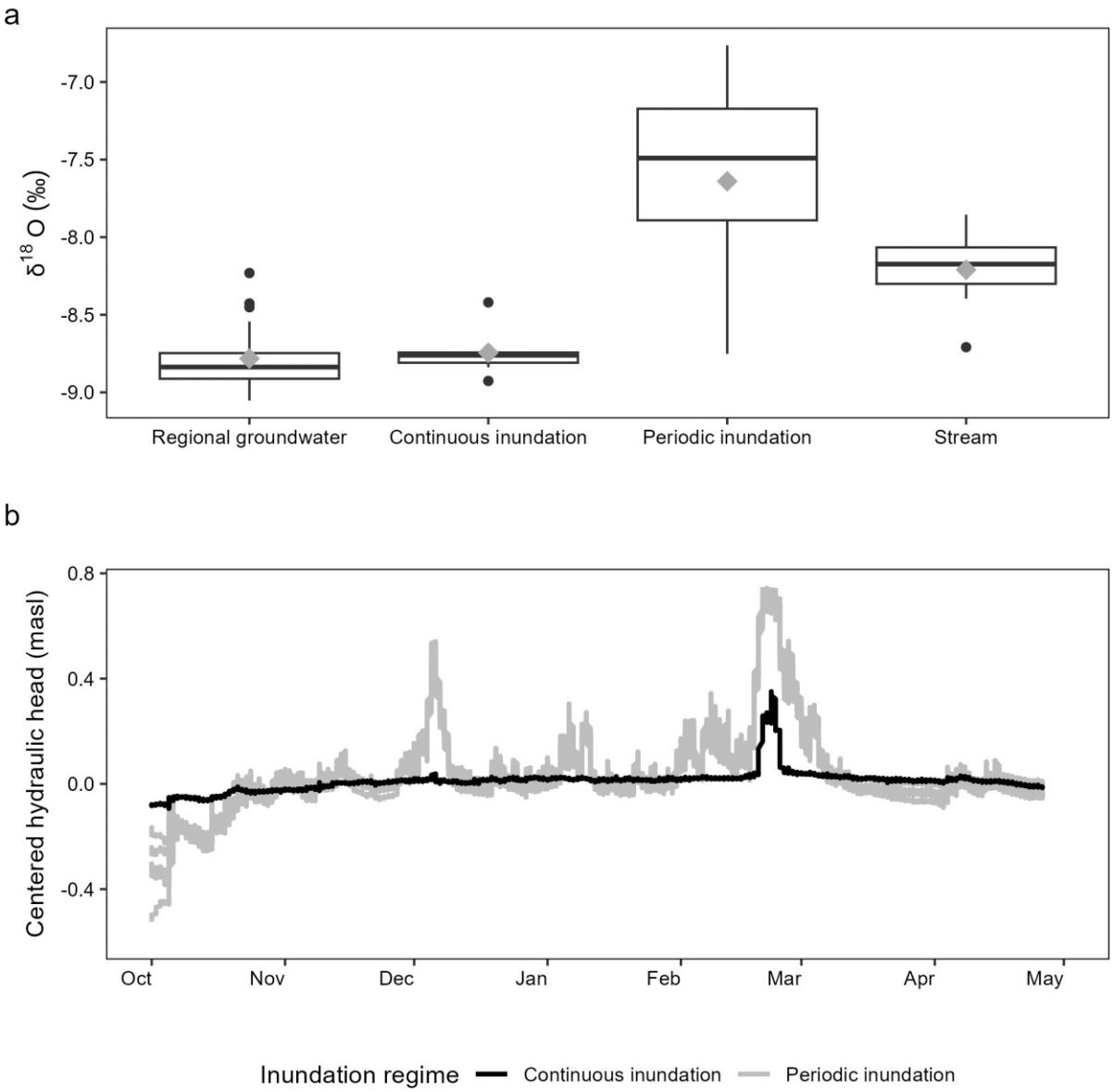

Figure 2. (a) From left to right: $\delta^{18}O$ isotopic signature of the regional groundwater (porewater from deep wells), shallow wells and piezometers from sites with respectively periodic and continuous inundation and water from Tryggevælde stream. Boxes contain the data's 25th to 75th percentile (the interquartile range, IQR) with the horizontal line within the box marking the median and grey diamonds indicating the mean. Whiskers mark data within 1.5 IQR and data points outside this range are shown as individual points. (b) Centered hydraulic head (values subtracted by the mean) in meters above sea level (masl) from October 2021 to April 2022. The black line indicates the hydraulic head in the shallow well placed in the area with continuous inundation (CI) and the grey lines represent the five shallow wells from the area with periodic inundation (PI).

3.2 Environmental conditions

During the six sampling campaigns for chamber based GHG flux measurements between autumn 2021 and early summer 2022, the soil temperature ranged between 4.0 and 14.9 °C (mean 8.9 °C). The mean water depth in CI and PI were similar, but the water level was more stable in the former (CI 8.5, range 6-16 cm; PI: mean 9.5, range 3-23 cm). Average wind speeds were generally low during the chamber deployments (mean 1.7 m s^{-1}, range 0-6.8 m s^{-1}) with a maximum gust speed of 12.4 m s^{-1} (mean 4.4 m s^{-1}, Fig. S1). PAR ranged between 0 and 1465 µmol m^{-2} s^{-1} (mean 337 µmol m^{-2} s^{-1} during daytime).

3.3 Effluxes of CH_4 and CO_2 from continuously and periodically inundated areas

The mean total CH_4 flux across sites was 0.16 g CH_4-C m^{-2} d^{-1}, but the temporal variation between days was extensive (range −0.028-1.66 g CH_4-C m^{-2} d^{-1}) with the highest fluxes in May and the lowest in February (Fig. 3a). Overall, there was a significantly higher total CH_4 flux in CI compared to PI (0.188 and 0.121 g CH_4-C m^{-2} d^{-1}, Welch t-tests $p < 0.001$, Fig. 4a). CI also had more frequent ebullitive events with at least one detectable ebullitive event in 54 % of the measurement cycles compared to only 4.6 % of the measurements in PI. For diffusive CH_4 fluxes values were higher from PI (0.12 g CH_4-C m^{-2} d^{-1}) compared to CI sites (0.075 g CH_4-C m^{-2} d^{-1}, Welch t-test, $p < 0.001$). Without considering any other covariates there was a diurnal variation in total CH_4 fluxes with significantly higher daytime (mean 0.173 g CH_4-C m^{-2} d^{-1}, Fig. 5) than nighttime fluxes (mean 0.151 g CH_4-C m^{-2} d^{-1}, Welch t-test $p = 0.041$). Likewise, we found higher daytime diffusive (mean 0.112 g CH_4-C m^{-2} d^{-1}) compared to nighttime fluxes (mean 0.0867 g CH_4-C m^{-2} d^{-1}, Welch t-test $p < 0.001$).

The overall mean CO_2 efflux was 1.23 g C m^{-2} d^{-1} (range −0.41-5.05 g C m^{-2} d^{-1}). The highest fluxes were observed in June 2021 (Fig. 3b). February had the lowest monthly flux (mean 0.47 g C m^{-2} d^{-1}) comprising only about 20 % of the rates in May and June. The few negative CO_2 fluxes (i.e uptake from the atmosphere) were observed in February (3 observations) and October (1 observation). In contrast to CH_4, the mean CO_2 flux was twice as high in PI (1.65) compared to CI (0.849 g C m^{-2} d^{-1}, Welch t-tests $p < 0.001$, Fig. 4b). Without taking covariates into account, daytime fluxes were higher than nighttime fluxes (daytime mean 1.45 and nighttime mean 1.08 g C m^{-2} d^{-1}, Welch t-test $p <. 0.001$, Fig. 5b).

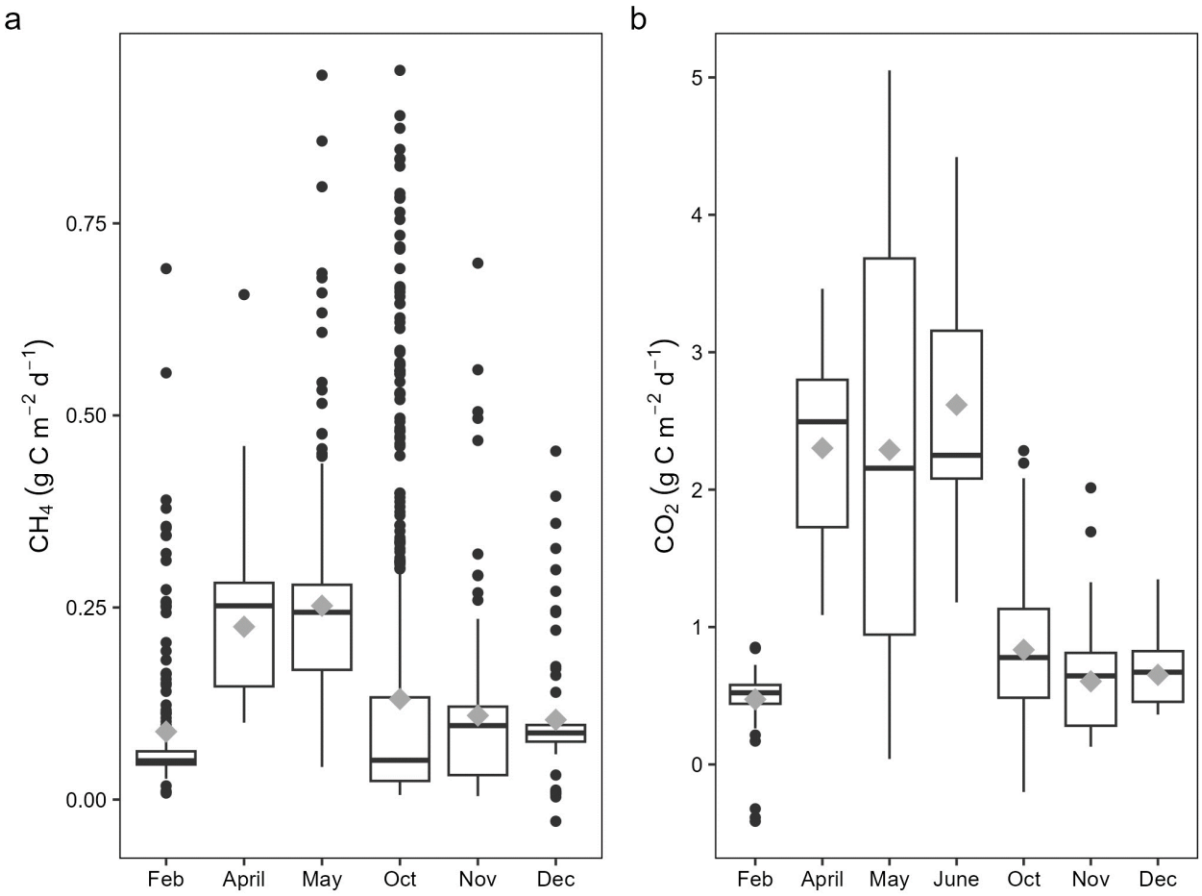

Figure 3. Seasonal variation in GHG effluxes. (a) Total CH_4 (diffusive + ebullitive), and (b) total (only diffusive) CO_2 flux in g C m^{-2} d^{-1}, grouped by month. Boxes contain the data's 25th to 75th percentile (the interquartile range, IQR) with the horizontal line within the box marking the median and grey diamonds indicating the mean. Whiskers mark data within 1.5 IQR and data points outside this range are shown as individual points. Seven CH_4 effluxes in May, September and October at 1.0-1.7 g C m^{-2} d^{-1} exceeding the upper range are omitted for clarity.

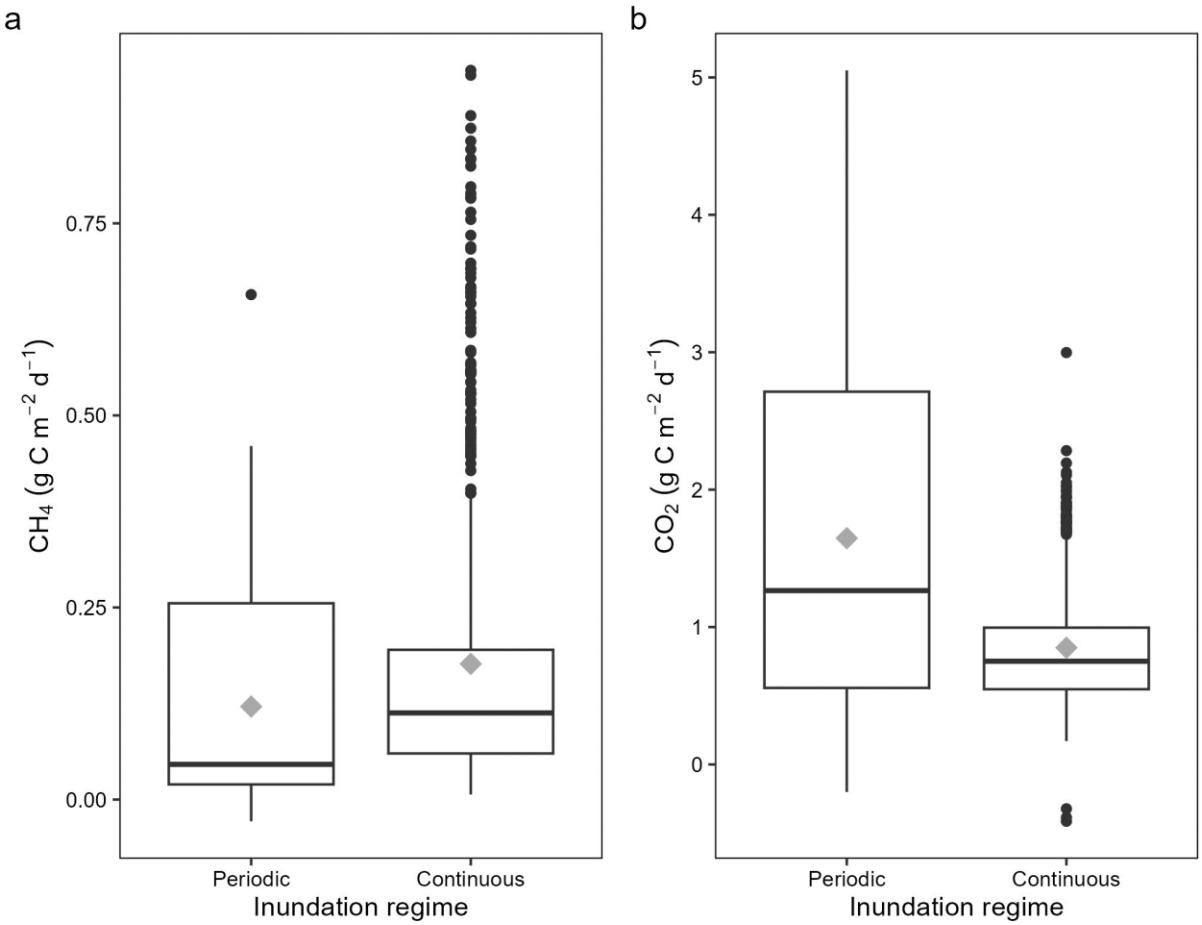

Figure 4. Boxplots of (a) total (diffusive + ebullitive) CH_4 flux and (b) total (only diffusive) CO_2 flux (g C m^{-2} d^{-1}) grouped by inundation regime. Boxes contain the data's 25th to 75th percentile (the interquartile range, IQR) with the horizontal line within the box marking the median and grey diamonds indicating the mean. Whiskers mark data within 1.5 IQR and data points outside this range are individual points. Seven CH_4 effluxes from CI at 1.0-1.7 g CH_4-C m^{-2} d^{-1} exceeding the upper range are omitted for clarity. Welch's t-tests showed a significant difference between CI and PI for both CH_4 and CO_2 ($p < 0.001$).

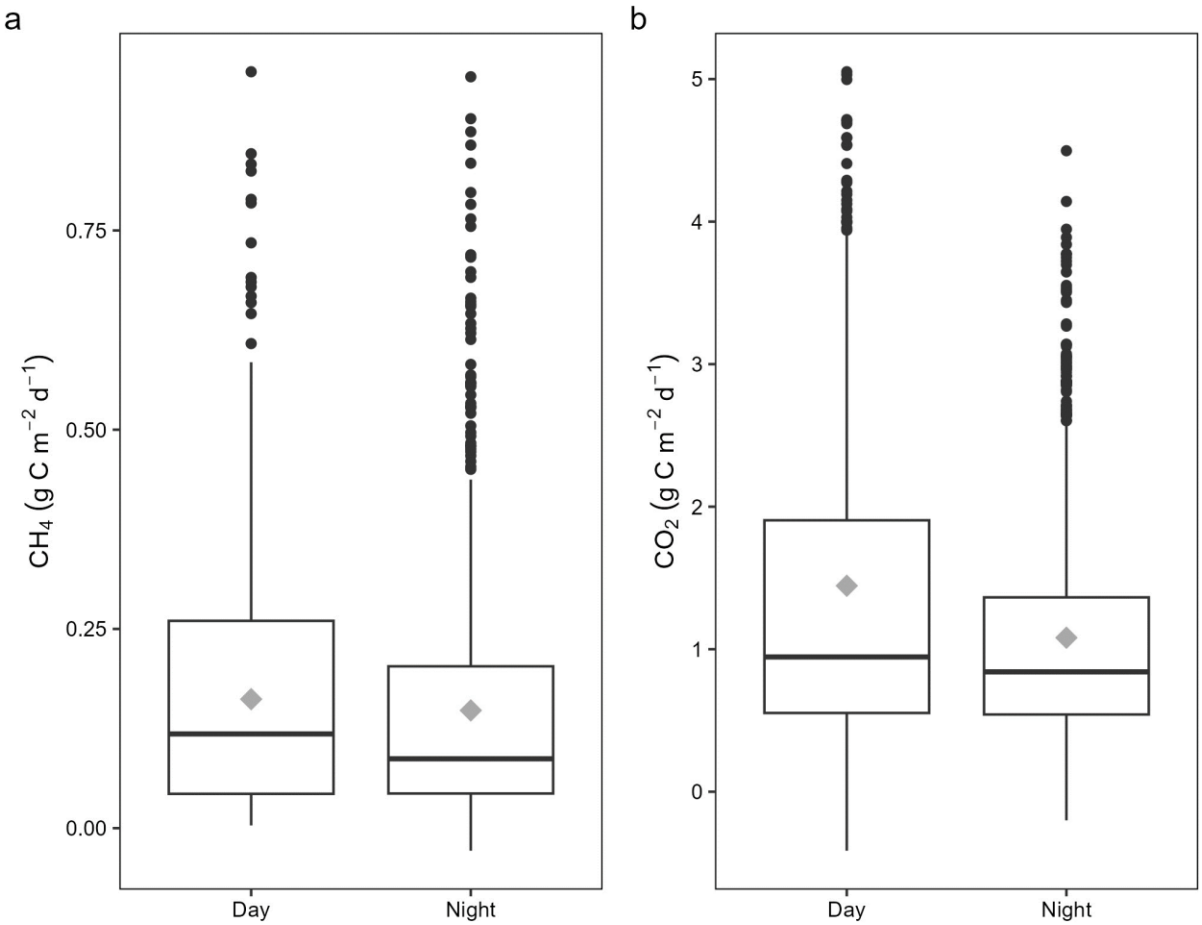

Figure 5. Boxplots showing diurnal variation between day and night for (a) total (diffusive + ebullitive) CH_4 flux and (b) total (only diffusive) CO_2 flux in g C m^{-2} d^{-1}. Boxes contain the data's 25th to 75th percentile (the interquartile range, IQR) with the horizontal line within the box marking the median and grey diamonds indicating the mean. Whiskers mark data within 1.5 IQR and data points outside this range are individual points. Seven CH_4 effluxes at 1.0-1.7 g CH_4-C m^{-2} d^{-1} exceeding the upper range are omitted for clarity. Welch's t-tests showed a significant ($p > 0.05$) difference between day and night, with higher daytime effluxes for both total CH_4 and CO_2.

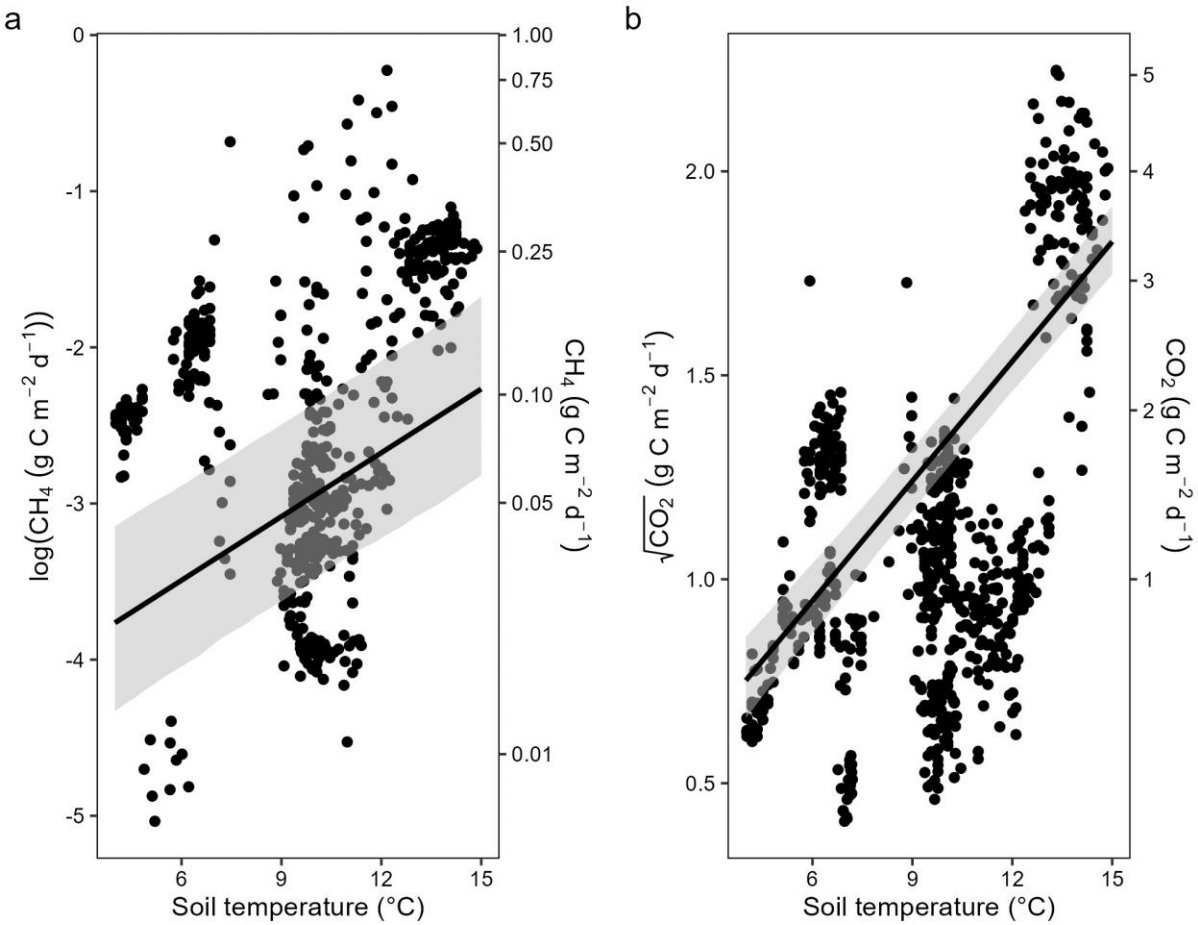

Figure 6. Fluxes of (a) total (diffusive + ebullitive) CH_4 and (b) total (only diffusive) CO_2 plotted against soil temperature. Lines and 95 % confidence intervals (grey shaded) from the model estimates.

3.4 Drivers of CH_4 and CO_2 effluxes

Using linear mixed-effects models on the subset containing complete environmental data showed that total CH_4 flux, diffusive CH_4 flux and CO_2 flux increased significantly with wind speed and soil temperature (table 1, Fig. 6). The models for total CH_4 and CO_2 fluxes confirmed the significant differences in fluxes between CI and PI, with higher total CH_4 flux in CI and higher CO_2 flux in PI. Contrary to the pairwise comparison, there were no significant differences between site types in the model for diffusive CH_4 flux. The diffusive CH_4 and CO_2 model showed a significant difference between day and night, with higher fluxes during nighttime, but no significant diurnal variation for total CH_4.

Among the included terms, there was a significant positive interaction between water depth and wind speed in the CO_2 flux model indicating that wind speed had larger effect on the CO_2 flux at higher water depths. Also, we observed a significant positive interaction between water depth

and soil temperature for all models, showing that increased soil temperature had a larger influence on gas fluxes in deeper water. The fixed effects explained approximately 50 % of the variation for the total CH_4 model (marginal R^2), 60 % for the diffusive CH_4 model and 75 % for the CO_2 model. Including plots as a random factor increased the amount of explained variation although not drastically (conditional R^2, table 1).

Table 1. Mixed linear models with total (diffusive + ebullitive) CH_4 flux (log transformed), diffusive CH_4 flux (square root transformed) and CO_2 flux (square root transformed) as the response variable, and 95 % bootstrapped confidence interval, for each predictor and interaction term. Confidence intervals in bold do not contain 0 and these predictors are considered significant. Continuous predictor variables were scaled to make it easier to compare the effects.

	Total CH_4		**Diffusive CH_4**		**CO_2**	
Predictor	*Estimates*	*Conf. Int.*	*Estimates*	*Conf. Int.*	*Estimates*	*Conf. Int.*
Soil temperature (°C)	0.37	**0.28 - 0.46**	0.042	**0.034 - 0.052**	0.27	**0.24 - 0.30**
Depth (cm)	0.33	**0.25 - 0.41**	0.061	**0.052 - 0.069**	−0.00027	−0.028 - 0.028
Wind speed (m s^{-1})	0.21	**0.14 - 0.29**	0.029	**0.022 - 0.037**	0.14	**0.13 – 0.17**
Continuous inundation	0.91	**0.11 - 1.78**	0.013	−0.071 - 0.95	-0.30	**−0.41 - −0.19**
Nighttime	0.067	−0.027 - 0.16	0.017	**0.0070 - 0.026**	0.059	**0.028 - 0.091**
Depth × Wind speed	0.069	−0.012 - 0.16	0.0026	−0.007 - 0.012	0.051	**0.020 - 0.080**
Soil temp. × Nighttime	−0.0027	−0.088 - 0.086	−0.0021	−0.012 - 0.0073	−0.030	−0.063 - 0.0039
Soil temp. × Depth	0.31	**0.17 - 0.44**	0.070	**0.056 - 0.086**	0.50	**0.46 - 0.54**
N	6 plots		6 plots		5 plots	
Observations	570		570		716	
Marginal R^2 / Conditional R^2	0.45 / 0.72		0.55 / 0.75		0.74 / 0.76	

3.5 Groundwater CH_4, CO_2, S^{2-}, O_2 and bubble formation pressures

Both CH_4 and CO_2 were exceedingly supersaturated at both CI and PI, with higher concentrations of both gases in the PI wells (table 2). Nevertheless, bubble formation pressures P_b were negative in the CI site (table 2) and only occasionally near-zero in the PI site. This

finding suggests that the ebullitive events of primarily CH_4 at the CI site observed with surface chambers were not a result of bubbles formed during depressurizing of upwelling groundwater.

The calculated diffusive groundwater-associated fluxes (F_{diff}^{gw}) showed a similar pattern to that of the concentrations with the higher fluxes in the PI site (table 2). However, for both CH_4 and CO_2 the groundwater-associated diffusive fluxes were insignificant relative to the total GHG emission, constituting respectively 0.007 % and 0.6 % of the measured effluxes from the water surface in the PI area, and 1.2×10^{-6} % and 0.2 % in the CI area. The groundwater's advective CH_4 and CO_2 fluxes (F_{adv}^{gw}) in the CI area were higher, amounting to 0.13 % and 2 %, respectively, but still negligible compared to the chamber-determined surface effluxes.

Advective groundwater-associated sulfide fluxes, which could result in consumption of molecular oxygen exceeded diffusive groundwater-associated sulfide fluxes in the CI area. Also, groundwater-associated diffusive fluxes were higher at the PI than at the CI sites (table 2). For oxygen, a downwards diffusive mean flux of 10 µmol m^{-2} d^{-1} was estimated.

Table 2. Groundwater concentrations, diffusive and advective fluxes of CO_2, CH_4, and S^{2-} and groundwater bubble formation pressure P_b (negative values indicate no potential bubble formation) from CI and PI. Numbers are means ± standard deviation. At atmospheric equilibrium (assuming 2 ppm CH_4 and 420 ppm CO_2 in the atmosphere) and ambient temperature, CH_4 and CO_2 has a concentration of 2.8 nM and 0.014 mM.

	CI	PI
[CO_2] mM	0.69 ± 0.26	2.0 ± 0.82
F_{diff}^{gw} mg CO_2-C m^{-2} d^{-1}	0.16 ± 0.20	1.0 ± 0.43
F_{adv}^{gw} mg CO_2-C m^{-2} d^{-1}	17 ± 25	-
[CH_4] µM	5.7 ± 6.1	16 ± 16
F_{diff}^{gw} µg CH_4-C m^{-2} d^{-1}	2.2 ± 3.2	8.5 ± 8.1
F_{adv}^{gw} µg CH_4-C m^{-2} d^{-1}	240 ± 341	-
[S^{2-}] µM	25 ± 45	82 ± 69
F_{diff}^{gw} µmol S^{2-} m^{-2} d^{-1}	1.1 ± 1.9	3.5 ± 3.0
F_{adv}^{gw} µmol S^{2-} m^{-2} d^{-1}	57 ± 82	-
P_b atm	−0.17 ± 0.017	−0.071 ± 0.061

4. Discussion

4.1 Local hydrology impacts GHG effluxes

The CO_2 effluxes from water surfaces were significantly higher in the lower part of the fen with periodic inundation (PI) compared to the continuously inundated (CI) areas with groundwater upwelling. In contrast, CH_4 effluxes were higher in the CI areas. This finding accords with our hypothesis that continuous soil saturation favors methanogenic activity leading to higher CH_4 effluxes, while periodic soil saturation favors aerobic and anaerobic microbial respiration releasing CO_2. Our results are in agreement with earlier research which has found similar patterns when comparing intermittently and continuously inundated wetlands (Juutinen et al., 2001; Qian et al., 2022; Song et al., 2003).

The groundwater upwelling into the CI site supported only small advective and diffusive CH_4 fluxes (i.e., F_{adv}^{gw} and F_{diff}^{gw}). Also, the bubble formation pressures in the CI area were negative. Thus, the surplus of CH_4 released to the atmosphere compared to the PI site must represent local production closer to the soil surface, i.e. at a more shallow depth than that of the well screens' which were localized at a depth of 0.5-0.8 mbgl.

A possible mechanism for the differences between PI and CI sites could be that continuous inundation depletes alternative electron acceptors from the CI site and creates stable anoxic conditions that favor methanogenic activity. Likewise, the onset of methanogenesis in rice fields has been found to be delayed several weeks after inundation (Yagi & Minami, 1993). Soil anoxia develops in a matter of hours after inundation, but methanogenesis is delayed until the microbial community has depleted the pool of energetically more favorable electron acceptors (nitrate, Mn^{4+}, Fe^{3+}, sulfate) produced during the unsaturated oxic period. This could explain the higher CH_4 and lower CO_2 effluxes at CI compared with PI. Supporting this explanation, a study investigating the effect of subsoil irrigation showed that a higher, stable groundwater level decreased oxygen intrusion and tended to deplete porewater Fe^{3+} and sulfate, while groundwater fluctuation stimulated electron acceptor renewal and inhibited CH_4 production (Boonman et al., 2023, PREPRINT).

In the CI site, the groundwater-associated advective sulfide flux appears adequate to help maintain methanogenic conditions near the soil surface. Upon oxidation to sulfate, one mole of H_2S corresponds to the release of 8 moles e^-. Reduction of one mole O_2 likewise corresponds to the acceptance of 4 moles e^-. Accordingly, the calculated upwards H_2S flux of 57 µmol m^{-2} d^{-1} (450 µmol e^- equivalents) easily outcompetes the downwards oxygen flux of 10 µmol m^{-2} d^{-1} (40 µmol e^- equivalents).

Inoculation with sediment rich in methanogens has been shown to drastically increase methane production under certain conditions, suggesting that the methane production may be limited by the density of methanogens and not by suitable organic substrates (Emilson et al., 2018). The abundance of methanogens might be higher under the stable anoxic conditions in CI relative to PI. Differences in sediment chemistry related to litter quality may also influence methanogenic activity (Emilson et al., 2018). However, there was no indication that litter quality differed substantially between the CI and PI sites, given the proximity, identical management and the highly organic soil at both sites.

4.2 Ebullition drives the difference in CH_4 efflux between sites

Despite the higher total CH_4 flux from CI, the diffusive CH_4 flux tended to be lower than at PI. Thus, the higher total efflux at CI can be attributed to substantial ebullition, which was virtually absent in PI. This is in line with a recent study showing that the difference between sites with differing hydrology in a temperate marsh is driven by ebullition and not diffusion (Villa et al., 2021). While diffusion is a slow process in saturated conditions, high CH_4 production and subsequent ebullition bypasses oxidation in oxic surface soils or water and can lead to high efflux rates (Sø et al., 2023, submitted). The spatial variability and high rates of CH_4 ebullition at CI emphasize the importance of using methods that capture stochastic ebullition events reliably over several days.

4.3 Other drivers of GHG effluxes

The diffusive gas flux is the product of the air-water concentration gradient and the gas transfer velocity. The gas transfer velocity is mainly driven by surface wind shear and convection. Differences in the diffusive gas flux due to increased gas transfer velocity are likely when the inundated area is large (Poindexter et al. 2016) because of higher wind fetch. This is supported in our data by the significant interaction between wind speed and water depth (highly correlated with inundated area) in the CO_2 model. Further, the higher CO_2 and diffusive CH_4 fluxes in the larger PI areas compared to the small inundated depressions in CI protected from wind shear also supports this effect. High wind shear and associated high diffusive flux will over time deplete the storage of dissolved CH_4 and, thus, the efflux. The time-integrated diffusive fluxes will ultimately be driven by the balance of CH_4 production and consumption in the oxic layers.

In agreement with numerous studies, we found a positive relationship between soil temperature and both CO_2 and CH_4 effluxes (Tiemeyer et al., 2020; Yvon-Durocher et al., 2014), probably due to an increased microbial activity by surface heating. Groundwater upwelling stabilizes temperatures (Bredehoeft & Papaopulos, 1965) and hence would counteract a relationship between soil temperature and GHG effluxes. Accordingly, the emitted GHGs are produced near the surface, also in the CI area, rather than being derived from the GHG contents of upwelling

groundwater. There was a very high degree of supersaturation of CH_4 and CO_2 in the groundwater, albeit bubbling formation pressures remained negative, but we found no meaningful contribution of neither diffusive nor advective flux from the groundwater. The CH_4 concentration in the groundwater is within the range observed in a study on potential CH_4 emissions from groundwater, yielding consistent findings of negligible contributions to overall CH_4 emissions (Gooddy & Darling, 2005).

Although the GHG fluxes were slightly higher during the daytime, statistical modeling suggested that when taking other variables like wind speed and soil temperature into account, we found the opposite pattern with significantly higher diffusive CH_4 and CO_2 effluxes during the night. For CO_2 the obvious explanation is that photosynthesis during daytime reduced the efflux compared to nighttime where respiration solely occurs. Other studies have found varying diurnal patterns for CH_4 including no diurnal variation and higher or lower effluxes during the day (Bansal et al., 2018; Sieczko et al., 2020). Our results suggests, that even when the diurnal variation is small, high frequency measurements are still needed, since ebullition events are highly stochastic and constitute a large proportion of the CH_4 efflux in CI. Automated and vented chambers or techniques that avoid any disturbance when placing the chambers are essential as trampling may provoke ebullition and corrupt measurements, particularly in peatland soils.

4.4 Conclusion

GHG fluxes from inundated areas are an important part of the wetland carbon budget. Our results showed that local hydrology can generate conditions that favor contrasting microbial degradation pathways at small spatial scales leading to opposite efflux patterns for the two GHGs CO_2 and CH_4. Combining surface measurements of gas fluxes with data on groundwater discharge and concentrations of GHGs revealed that virtually all of the gas efflux is caused by surface-near production with the hydrology structuring the abiotic conditions rather than driving the flux directly. The influence of local hydrology and high spatial variability highlights the importance of considering the spatial design and sampling frequency in chamber-based GHG studies. Future studies, which besides hydrological monitoring, combines frequent chamber measurements in drier periods and areas with high-frequency floating chamber measurements in the wet season, could generate reliable annual estimates.

Acknowledgements

This work was supported by grants to Kaj Sand-Jensen from the Independent Research Fund Denmark. We thank A. A. Bjørk for contributing the September 2021 aerial composite photo.

Data Availability Statement

https://erda.ku.dk/archives/986e112c425ccdc28c60a2ed56ead0a0/published-archive.html (will change to DOI upon acceptance)

References

Appelo, C. A. J., & Postma, D. (2005). *Geochemistry, Groundwater and Pollution* (2nd ed.). CRC Press. https://doi.org/10.1201/9781439833544

Bansal, S., Tangen, B., & Finocchiaro, R. (2018). Diurnal Patterns of Methane Flux from a Seasonal Wetland: Mechanisms and Methodology. *Wetlands*, *38*(5), 933–943. https://doi.org/10.1007/s13157-018-1042-5

Barbosa, P. M., Melack, J. M., Amaral, J. H. F., Linkhorst, A., & Forsberg, B. R. (2021). Large Seasonal and Habitat Differences in Methane Ebullition on the Amazon Floodplain. *Journal of Geophysical Research: Biogeosciences*, *126*(7), e2020JG005911. https://doi.org/10.1029/2020JG005911

Bartoń, K. (2023). *MuMIn: Multi-Model Inference* (1.47.5) [Software]. https://cran.r-project.org/web/packages/MuMIn/index.html

Bastviken, D., Nygren, J., Schenk, J., Parellada Massana, R., & Duc, N. T. (2020). Technical note: Facilitating the use of low-cost methane (CH_4) sensors in flux chambers – calibration, data processing, and an open-source make-it-yourself logger. *Biogeosciences*, *17*(13), 3659–3667. https://doi.org/10.5194/bg-17-3659-2020

Bates, D., Mächler, M., Bolker, B., & Walker, S. (2015). Fitting Linear Mixed-Effects Models Using lme4. *Journal of Statistical Software*, *67*, 1–48. https://doi.org/10.18637/jss.v067.i01

Boonman, J., Harpenslager, S. F., van Dijk, G., Smolder, A. J. P., Hefting, M. M., van de Riet, B., & van der Velde, Y. (2023). *Peatland porewater chemistry reveals field redox ranges for specific decomposition processes* [Preprint], https://doi.org/10.21203/rs.3.rs-2845768/v1.

Bredehoeft, J. D., & Papaopulos, I. S. (1965). Rates of vertical groundwater movement estimated from the Earth's thermal profile. *Water Resources Research*, *1*(2), 325–328. https://doi.org/10.1029/WR001i002p00325

Cline, J. D. (1969). Spectrophotometric Determination of Hydrogen Sulfide in Natural Waters1. *Limnology and Oceanography*, *14*(3), 454–458. https://doi.org/10.4319/lo.1969.14.3.0454

Ding, W., Cai, Z., & Tsuruta, H. (2004). Diel variation in methane emissions from the stands of Carex lasiocarpa and Deyeuxia angustifolia in a cool temperate freshwater marsh. *Atmospheric Environment*, *38*(2), 181–188. https://doi.org/10.1016/j.atmosenv.2003.09.066

Emilson, E. J. S., Carson, M. A., Yakimovich, K. M., Osterholz, H., Dittmar, T., Gunn, J. M., Mykytczuk, N. C. S., Basiliko, N., & Tanentzap, A. J. (2018). Climate-driven shifts in sediment chemistry enhance methane production in northern lakes. *Nature Communications*, *9*(1), Article 1. https://doi.org/10.1038/s41467-018-04236-2

Gooddy, D. C., & Darling, W. G. (2005). The potential for methane emissions from groundwaters of the UK. *Science of The Total Environment*, *339*(1–3), 117–126. https://doi.org/10.1016/j.scitotenv.2004.07.019

Henneberger, R., Cheema, S., Folini, M., & Zeyer, J. (2017). Diurnal Patterns of Greenhouse Gas Fluxes in a Swiss Alpine Fen. *Wetlands*, *37*(2), 193–204. https://doi.org/10.1007/s13157-016-0844-6

Jerman, V., Metje, M., Mandić-Mulec, I., & Frenzel, P. (2009). Wetland restoration and methanogenesis: The activity of microbial populations and competition for substrates at different temperatures. *Biogeosciences*, *6*(6), 1127–1138. https://doi.org/10.5194/bg-6-1127-2009

Juutinen, Alm, Martikainen, & Silvola. (2001). Effects of spring flood and water level draw-down on methane dynamics in the littoral zone of boreal lakes. *Freshwater Biology*, *46*(7), 855–869. https://doi.org/10.1046/j.1365-2427.2001.00721.x

Leifeld, J., & Menichetti, L. (2018). The underappreciated potential of peatlands in global climate change mitigation strategies. *Nature Communications*, *9*(1), Article 1. https://doi.org/10.1038/s41467-018-03406-6

Martin, R. M., & Moseman-Valtierra, S. (2017). Plant manipulations and diel cycle measurements test drivers of carbon dioxide and methane fluxes in a Phragmites australis-invaded coastal marsh. *Aquatic Botany*, *137*, 16–23. https://doi.org/10.1016/j.aquabot.2016.11.003

Martinsen, K. T., Kragh, T., & Sand-Jensen, K. (2018). Technical note: A simple and cost-efficient automated floating chamber for continuous measurements of carbon dioxide gas flux on lakes. *Biogeosciences*, *15*(18), 5565–5573. https://doi.org/10.5194/bg-15-5565-2018

Moore, T. R., & Knowles, R. (1990). Methane emissions from fen, bog and swamp peatlands in Quebec. *Biogeochemistry*, *11*(1), 45–61. https://doi.org/10.1007/BF00000851

Pekel, J.-F., Cottam, A., Gorelick, N., & Belward, A. S. (2016). High-resolution mapping of global surface water and its long-term changes. *Nature*, *540*(7633), Article 7633. https://doi.org/10.1038/nature20584

Qian, H., Chen, J., Zhu, X., Wang, L., Liu, Y., Zhang, J., Deng, A., Song, Z., Ding, Y., Jiang, Y., van Groenigen, K. J., & Zhang, W. (2022). Intermittent flooding lowers the impact of elevated atmospheric CO2 on CH4 emissions from rice paddies. *Agriculture, Ecosystems & Environment*, *329*, 107872. https://doi.org/10.1016/j.agee.2022.107872

R Core Team. (2023). *R: A language and environment for statistical computing.* [Software]. R Foundation for Statistical Computing. https://www.R-project.org/.

Scharlemann, J. P., Tanner, E. V., Hiederer, R., & Kapos, V. (2014). Global soil carbon: Understanding and managing the largest terrestrial carbon pool. *Carbon Management*, *5*(1), 81–91. https://doi.org/10.4155/cmt.13.77

Sieczko, A. K., Duc, N. T., Schenk, J., Pajala, G., Rudberg, D., Sawakuchi, H. O., & Bastviken, D. (2020). Diel variability of methane emissions from lakes. *Proceedings of the National Academy of Sciences*, *117*(35), 21488–21494. https://doi.org/10.1073/pnas.2006024117

Song, C., Yan, B., Wang, Y., Wang, Y., Lou, Y., & Zhao, Z. (2003). Fluxes of carbon dioxide and methane from swamp and impact factors in Sanjiang Plain, China. *Chinese Science Bulletin*, *48*(24), 2749–2753. https://doi.org/10.1007/BF02901769

Stanley, K. M., Heppell, C. M., Belyea, L. R., Baird, A. J., & Field, R. H. (2019). The Importance of CH4 Ebullition in Floodplain Fens. *Journal of Geophysical Research: Biogeosciences*, *124*(7), 1750–1763. https://doi.org/10.1029/2018JG004902

Sø, J. S., Martinsen, K. T., Kragh, T., & Sand-Jensen, K. (2023). *Ebullition dominates high lake methane emissions globally across all lake sizes* [Paper submitted for publication].

Sø, J. S., Sand-Jensen, K., Martinsen, K., Polauke, E., Kjær, J., Reitzel, K., & Kragh, T. (2022). Methane and Carbon Dioxide Fluxes at High Spatiotemporal Resolution from a Small Temperate Lake. I *SSRN Electronic Journal*. https://doi.org/10.2139/ssrn.4215178

Tiemeyer, B., Freibauer, A., Borraz, E. A., Augustin, J., Bechtold, M., Beetz, S., Beyer, C., Ebli, M., Eickenscheidt, T., Fiedler, S., Förster, C., Gensior, A., Giebels, M., Glatzel, S., Heinichen, J., Hoffmann, M., Höper, H., Jurasinski, G., Laggner, A., … Drösler, M. (2020). A new methodology for organic soils in national greenhouse gas inventories: Data synthesis, derivation and application. *Ecological Indicators*, *109*, 105838. https://doi.org/10.1016/j.ecolind.2019.105838

Villa, J. A., Ju, Y., Yazbeck, T., Waldo, S., Wrighton, K. C., & Bohrer, G. (2021). Ebullition dominates methane fluxes from the water surface across different ecohydrological patches in a temperate freshwater marsh at the end of the growing season. *Science of The Total Environment*, *767*, 144498. https://doi.org/10.1016/j.scitotenv.2020.144498

Wachinger, G., Fiedler, S., Zepp, K., Gattinger, A., Sommer, M., & Roth, K. (2000). Variability of soil methane production on the micro-scale: Spatial association with hot spots of organic material and Archaeal populations. *Soil Biology and Biochemistry*, *32*(8), 1121–1130. https://doi.org/10.1016/S0038-0717(00)00024-9

Yagi, K., & Minami, K. (1993). Spatial and Temporal Variations of Methane Flux from a Rice Paddy Field. I R. S. Oremland (Red.), *Biogeochemistry of Global Change: Radiatively Active Trace Gases Selected Papers from the Tenth International Symposium on Environmental Biogeochemistry, San Francisco, August 19–24, 1991* (s. 353–368). Springer US. https://doi.org/10.1007/978-1-4615-2812-8_19

Yu, Z., Loisel, J., Brosseau, D. P., Beilman, D. W., & Hunt, S. J. (2010). Global peatland dynamics since the Last Glacial Maximum. *Geophysical Research Letters*, *37*(13). https://doi.org/10.1029/2010GL043584

Yvon-Durocher, G., Allen, A. P., Bastviken, D., Conrad, R., Gudasz, C., St-Pierre, A., Thanh-Duc, N., & del Giorgio, P. A. (2014). Methane fluxes show consistent temperature dependence across microbial to ecosystem scales. *Nature*, *507*(7493), 488–491. https://doi.org/10.1038/nature13164

Zhang, H., Tuittila, E.-S., Korrensalo, A., Laine, A. M., Uljas, S., Welti, N., Kerttula, J., Maljanen, M., Elliott, D., Vesala, T., & Lohila, A. (2021). Methane production and oxidation potentials along a fen-bog gradient from southern boreal to subarctic peatlands in Finland. *Global Change Biology*, *27*(18), 4449–4464. https://doi.org/10.1111/gcb.15740